Research Article

Zhiyuan Wang, Long Chen*, Chenyang Zhu, Zhanqiang Liu, and Qinghua Song

Optimization method for low-velocity impact identification in nanocomposite using genetic algorithm

https://doi.org/10.1515/ntrev-2024-0067
received March 9, 2024; accepted July 6, 2024

Abstract: Fiber-reinforced plastic (FRP) is prone to invisible damage caused by low-velocity impact (LVI) during service. The structural health monitoring system is of great significance for damage monitoring and maintenance of composite materials. In this study, four fiber Bragg grating sensors were employed to collect the time domain strain signals of composite materials subjected to LVIs. Furthermore, a numerical simulation model was established to rapidly obtain impact signal dataset. The signal arrival time, peak time, and peak amplitude were selected as signal features, and the backpropagation neural network was successfully applied to determine the location and energy of LVIs. To address the issue of peak feature extraction in the strain signal processing, a genetic algorithm-based sliding window peak detection optimization method was proposed, which significantly improved the final prediction accuracy. The experimental results indicated that within a position range of 300 mm × 300 mm, the average positioning error can reach 5.1 mm; and in an energy range of 0.5–1 J, the average energy prediction error can reach 0.030 J. The proposed method achieved accurate identification of the LVI location and energy for FRP.

Keywords: fiber-reinforced plastic, fiber Bragg grating sensor, structural health monitoring, low-velocity impact, genetic algorithm, backpropagation neural network

*** Corresponding author: Long Chen**, Key Laboratory of High Efficiency and Clean Mechanical Manufacture, Ministry of Education, Jinan, China; School of Mechanical Engineering, Shandong University, Jinan, China; Key Laboratory of Icing and Anti/De-icing, China Aerodynamics Research and Development Center, Mianyang, China; Rizhao Institute of Shandong University, Rizhao, China, e-mail: 812612937@qq.com, tel: +86-531-88396208
Zhiyuan Wang, **Chenyang Zhu**, **Zhanqiang Liu**, **Qinghua Song:** Key Laboratory of High Efficiency and Clean Mechanical Manufacture, Ministry of Education, Jinan, China; School of Mechanical Engineering, Shandong University, Jinan, China

1 Introduction

Due to the advantages of lightweight, high strength, high rigidity, corrosion resistance, and fatigue resistance, fiber-reinforced plastic (FRP) has found extensive applications in various fields such as aerospace, automotive manufacturing, military, and construction materials [1,2]. However, during service, FRP is susceptible to damage from low-velocity impacts (LVIs) [3]. These damages are often difficult to detect by the naked eyes, and the damage mechanism is influenced by the impact energy and shape of the impactor [4,5], making it challenging for conventional detection methods to rapidly and accurately assess the damage situation. In response, structural health monitoring (SHM) has evolved to ensure the safe use of materials by establishing a distributed sensor network on the surface or within the composite material for the monitoring of structural health [6–9].

In recent years, researchers have performed a substantial amount of research work on SHM of composite materials. Katunin and Przystałka [10] employed fractional discrete wavelet transform and modal shape displacement for damage detection in composite material plates. Based on Lamb wave delamination scanning technology, Prasad *et al.* [11] introduced a composite material damage monitoring method. By considering the anisotropic and attenuation characteristics of composite plate, they obtained optimized delamination images of composite plate. Liu *et al.* [12] established an integrated distributed eddy current sensor network, successfully developing a method for quantitative prediction of hole edge damage in composite material bolted joints. de Castro *et al.* [13] studied the noise signal shielding capability of different signal processing methods in composite material damage determination based on electromechanical impedance technology. Saeedifar *et al.* [14] explored impact damage in different composite materials under quasi-static indentation and LVI loads using acoustic emission technology. Employing a multi-modal excitation approach based on vibration acoustic modulation technology, Loi *et al.* [15] achieved local damage detection in

composite beams successfully. These methods have utilized various signal processing techniques for the SHM of composite materials. However, challenges arise in practical engineering applications, particularly concerning feature extraction, pattern recognition, and rapid decision-making based on extensive data. These issues often present obstacles to traditional health monitoring methods.

Due to the powerful data processing capabilities, flexible adaptability, and strong predictive performance, machine learning is increasingly used to optimize SHM for composite materials [16]. Based on deep transfer learning techniques, Liu *et al.* [17] integrated monitoring data with physical mechanisms, proposing a stable and scalable structural damage detection framework for carbon fiber-reinforced plastic plates (CFRP). Moradi *et al.* [18] used semi-supervised deep neural networks for feature fusion of time and frequency domain characteristics of composite plate, extracting higher-quality intelligent health indicators. Johnson [19] employed principal component analysis (PCA) to effectively distinguish the acoustic emission responses of composite material matrix cracking and local delamination. A numerical program that utilizes the particle swarm optimization (PSO) technique was proposed by Jebieshia *et al.* [20]. It monitored and quantified damage in composite beams and plate-like structures by detecting changes in vibration response parameters caused by damage. Majumdar *et al.* [21] predicted damage locations and quantities in truss-like structures using ant colony optimization algorithms based on changes in the natural frequencies of composite materials. Using PCA to compress the frequency response data of materials, Zang and Imregun [22] employed artificial neural networks (ANN) to differentiate between the healthy and damaged states of composite materials. McCrory *et al.* [23] conducted research on the identification performance of three acoustic emission classification techniques: ANN, unsupervised waveform clustering (UWC), and modal assurance criterion. The results indicated the advantages of ANN and UWC in distinguishing between multiple damage categories. These methods have exhibited good reliability, but often necessitate external equipment and human involvement, resulting in high costs and difficulties in achieving the practical monitoring of structural health status.

Fiber Bragg grating (FBG) sensors, due to their advantages of high sensitivity, strong interference resistance, good flexibility, and multiplexing capability, are often combined with ANN for real-time SHM of FRP [24–27]. A binary dynamic stochastic search (BDSS)-support vector regression (SVR) positioning method was first introduced by Liu *et al.* [28], which combines the BDSS algorithm with SVR, effectively enhancing the accuracy of LVI positioning in composite materials. Califano *et al.* [29] introduced a real-time SHM method for composite structures based on ANN and FBG sensors. This method relies on the correlation of strains at various material locations and offers a lower computational cost. A composite material SHM system based on dynamic strain measurements was introduced by Panopoulou *et al.* [30]. The discrete wavelet transform was employed to extract joint time–frequency domain features from FBG sensor signals and an ANN was employed for damage location identification. It achieved an accuracy of 86% in location recognition. Shen and Tian [31] used PSO to optimize an ANN for the identification of static load locations in fiber-reinforced composite structures. Wen *et al.* [32] processed FBG sensor signals using fast Fourier transform and PCA techniques. They employed a backpropagation (BP) neural network to achieve impact positioning in CFRP, with an average positioning error of 21 mm. The SHM scheme based on FBG sensors and ANN has the advantages of high accuracy, fast response, and good adaptability, and the processing of FBG sensor signals is one of the keys to improve the monitoring performance.

Based on the above research, this article proposed a new method for the joint recognition of impact location and energy in FRP, utilizing FBG sensors and BP neural network. This method selects signal arrival time, peak time, and peak amplitude of the strain signals collected by FBG sensors during LVIs as signal features, and a BP neural network is employed for impact location and energy prediction. Furthermore, to address the issue of feature peak selection, a genetic algorithm (GA) is utilized to optimize the parameters of sliding window peak detection, resulting in a more representative peak feature extraction scheme. The results indicate that using signal arrival time, peak time, and peak amplitude as features enables the prediction of impact location and energy in FRP under LVIs. Furthermore, after using GA to optimize the parameters of sliding window peak detection, the accuracy of impact location and energy prediction reaches a high level.

The highlights and contributions of this study are as follows:

- A joint prediction scheme for LVI location and energy based on FBG sensors and BP neural network was designed. The normalization of input dataset was employed to mitigate the impact of feature scale differences on neural network training.
- Complex feature definitions were avoided, and the prediction of LVI on FRP was successfully achieved by using signal arrival time, peak time, and peak amplitude as features.
- The GA was innovatively employed to automatically search for an optimized feature peak extraction scheme. This significantly improved prediction results and enhanced the method's generalizability for addressing various engineering problems.

- The effectiveness of four different optimization algorithms in the optimization of signal feature peaks were compared, and the reason for differences in prediction performance was discussed.

The remaining sections of this article are structured as follows: In Section 2, an experimental system for LVI on FRP is set up, and simulations are performed on ANSYS Workbench 2023. This section also presents a detailed description of the initial selection of time-domain features to predict impact location and energy. Section 3 delves into the principles of the GA and provides evidence of the remarkable effects and unique advantages of applying GA to optimize peak feature extraction. Lastly, Section 4 offers the article's conclusion.

2 Preliminary prediction of LVI

2.1 Experimental setup

To investigate the response of composite materials to LVIs, an experimental setup for LVI on composite material plate was constructed, as shown in Figure 1(a). The experimental setup consisted of a composite material plate, a metal ball, four FBG sensors, fixtures, a grating demodulator, and a computer.

The composite material was manufactured using a hot press molding process. The lining was T300 unidirectional fabric (carbon fiber) produced by Japan Toray Industries, Inc., arranged in $[0/90]_{3s}$ cross-ply configuration with a thickness of 0.25 mm per layer. The plate had 12 layers in total. Resin was utilized as the adhesive agent. The composite material plate had dimensions of 500 mm × 500 mm × 3.5 mm and was fixed to the impact platform by fixing all four edges. To reduce the influence of boundary effects, the central area of the plate, measuring 300 mm × 300 mm, was designated as the testing area.

Four FBG sensors were single optical fiber sensors produced by Technica Optical Components, LLC (grating length: 10 mm, central wavelength: 1,555 ± 0.5 nm, strain range: >15,000 με, and sensitivity: 1.2 pm/με). They were fixed at the corners of the testing area using epoxy resin, as shown in Figure 1(b). Different LVIs in terms of location and energy were generated by adjusting the falling location and height of the ball (structural steel, R = 15 mm). Strain signals were collected by four FBG sensors. The high-speed demodulator operated at a frequency of 50 kHz. It was used to convert the input optical signal into the electrical signal and performed amplification, filtering, and digitization. The demodulated signals would be displayed on the computer.

Using the lower-left corner of the plate as the coordinate origin, the horizontal and vertical directions were defined as the x-axis and y-axis, respectively. In the initial experiment, the ball's location and height were adjusted at the coordinate (150 mm, 150 mm) with an energy of 0.5 J, defining these as the impact parameters (150, 150, 0.5). Wavelength displacement data from the first 500 sampling points of the four sensors were collected. Strain waveforms were plotted in MATLAB based on the provided sensor sensitivity, as shown in Figure 2.

2.2 Numerical simulation modeling and validation

To minimize experimental costs and quickly generate a dataset for LVIs at various locations and energies, finite

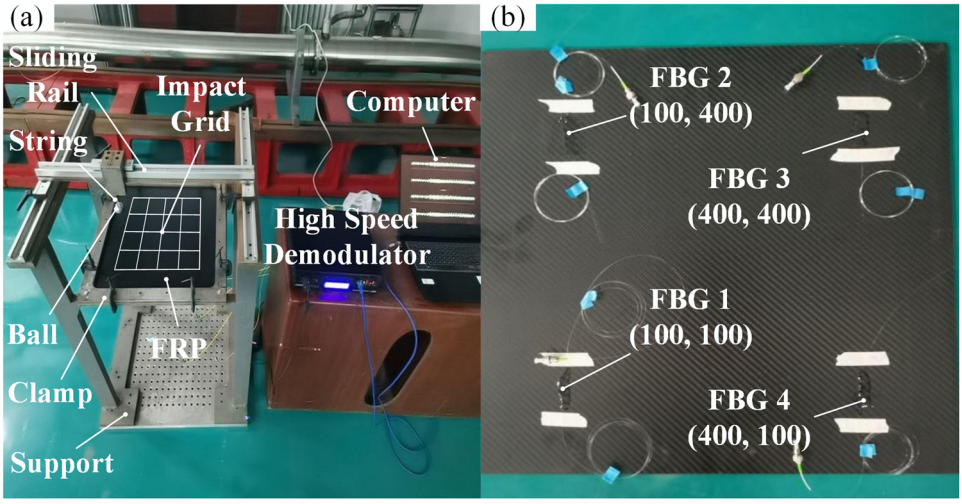

Figure 1: Composite material plate LVI experimental setup of (a) experimental platform and (b) sensor arrangement.

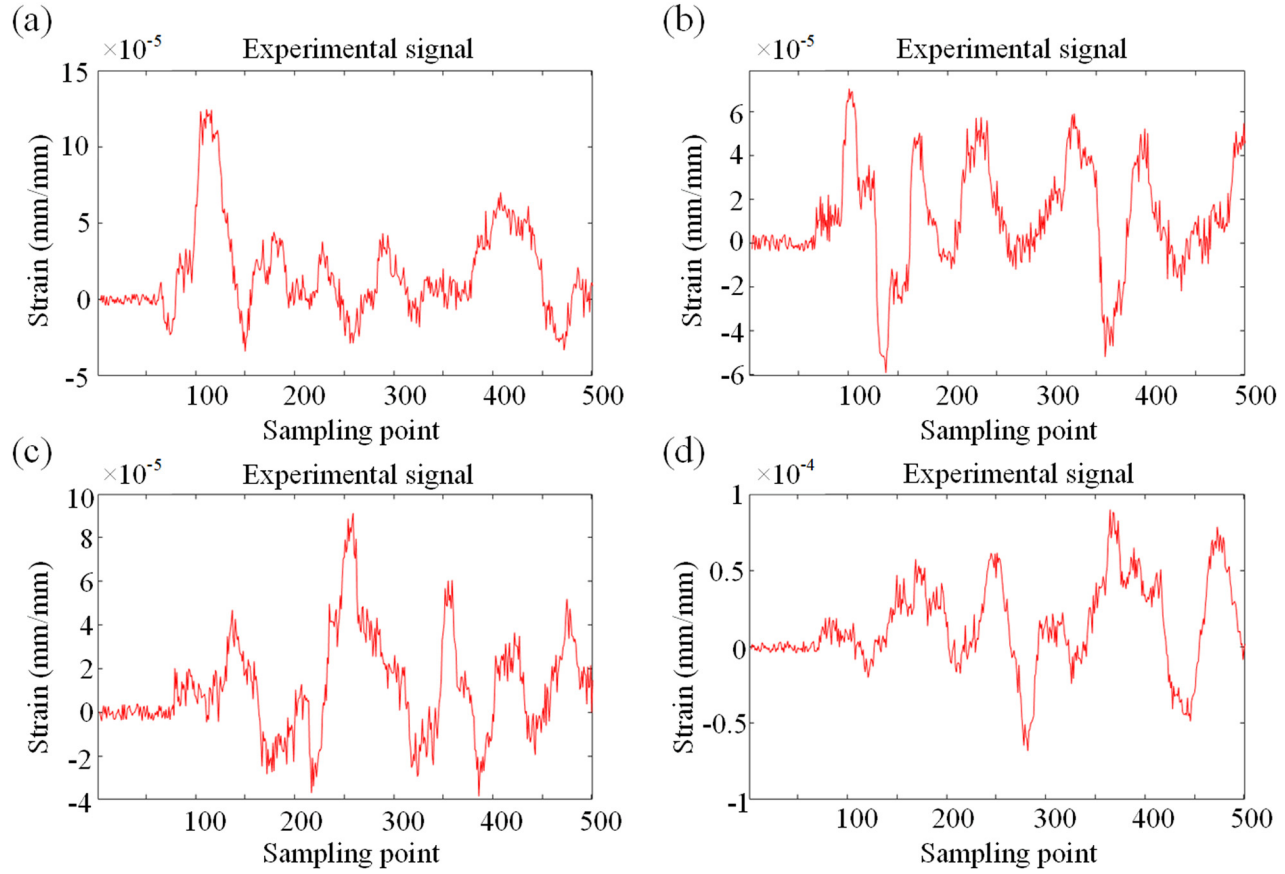

Figure 2: Strain waveforms of the composite plate at (a) FBG 1, (b) FBG 2, (c) FBG 3 and (d) FBG 4.

element simulations were performed using ANSYS Workbench 2023. The LVI behavior of a structural steel ball on the composite material plate was simulated. Table 1 shows the key properties of the carbon fiber fabric in the finite element model. The fabric follows the same stacking sequence and size as before. Figure 3 shows the geometric structure of the model. The boundary conditions were set as all sides were fixed to avoid disallowing displacement and rotation of the composite plate. Axial strain sensors were positioned at the corresponding locations on the composite material plate to collect strain signals.

Table 1: Key properties of the carbon fiber fabric

Property parameters	Value
Density	1,490 kg/m^{-3}
Young's modulus *X* direction	121 GPa
Young's modulus *Y/Z* direction	8.6 GPa
Poisson's ratio *YZ*	0.4
Poisson's ratio *XY/XZ*	0.27
Shear modulus *YZ* direction	3.1 GPa
Shear modulus *XY/XZ* direction	4.7 GPa

Proper mesh division is crucial for improving the accuracy and stability of numerical computations. The element sizes of the ball and the plate were set to 4 and 10 mm, respectively, using the peak time and amplitude (collected by sensor 1, with [150, 150, 0.5] as impact parameters) as indicators to conduct mesh independence verification. The results are shown in Figure 4. It can be observed that when element sizes of the ball and the plate were smaller than 4

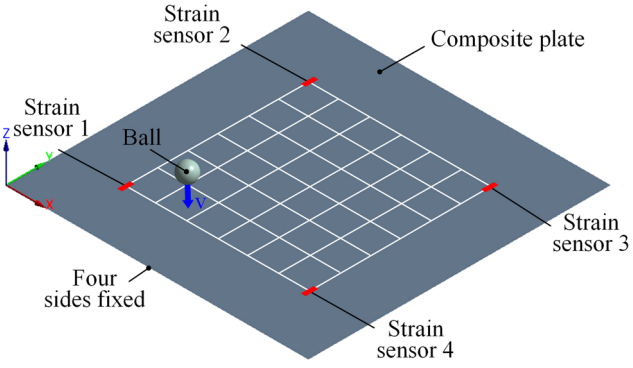

Figure 3: Geometric structure of LVI simulation model.

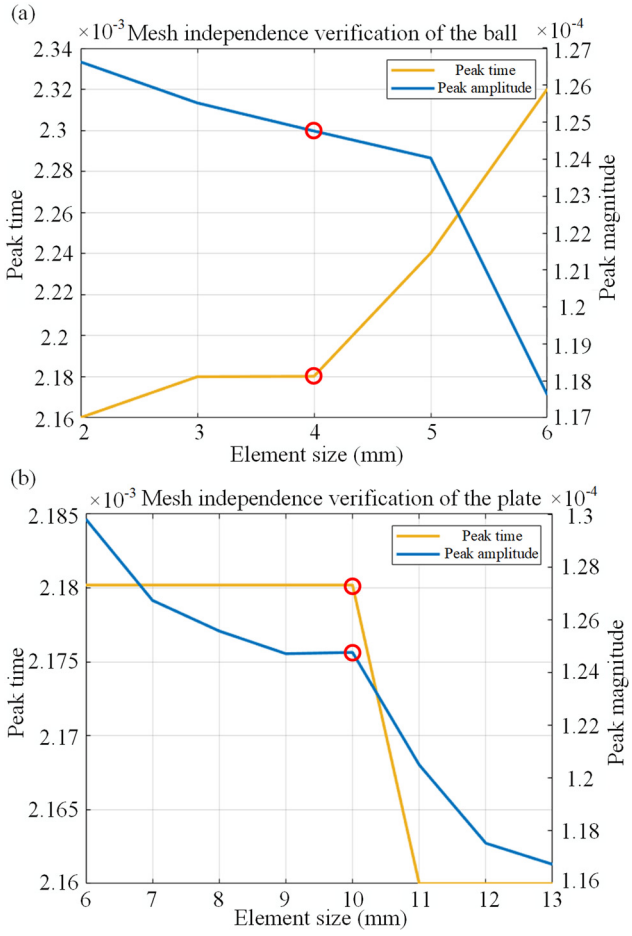

Figure 4: Mesh independence verification of (a) the ball and (b) the plate.

and 10 mm, respectively, the numerical calculation results showed minimal improvement with the refinement of the mesh. Considering both computational accuracy and efficiency, setting the element sizes to 4 and 10 mm, respectively, was the most appropriate. At this point, the average mesh quality of the model was 0.9193.

To validate the correctness of the simulation model, the same LVI parameters of (150, 150, 0.5) were set in the first impact. Time-domain strain signals collected by four strain sensors were used to calibrate the model. After fine-tuning the volume fraction and thickness of the fabric, and adjusting the solver analysis settings, the simulation data achieved higher accuracy, as shown in Figure 5. It can be observed that, compared to the experimental data, the simulation data exhibit fewer spikes and abrupt changes. However, the overall trends of the two curves are similar, and the rise time and peak-to-peak values also match well. The correlation coefficient measures the linear correlation between two waveforms and can be used to assess whether two waveforms are similar over time. Table 2 displays the correlation coefficients between the experimental and simulation signals at four positions. It can be seen that the correlation coefficients at each position are 0.8868, 0.9034, 0.8541, and 0.8231, respectively, all close to 1. This indicates a strong similarity between the two waveforms. Considering that the experimental signals were also influenced by factors such as temperature, noise, sensor accuracy, *etc.*, it can be concluded that the results of the simulation model are consistent with the real situation.

2.3 Construction of neural network training set

To construct a sufficiently large input dataset for the BP neural network to learn the patterns and correlations of input–output signals, 25 grid points were uniformly selected within the test area of the composite material plate as impact points. For each grid point, the ball impacted with energies of 0.5, 0.75, and 1.0 J, respectively. Consequently, the neural network's training set consisted of a total of 25 × 3 samples, as depicted in Figure 6.

The explicit dynamics module was used to solve each sample model, and the strain data were collected by four strain sensors. Figure 7(a) shows the signals captured by FBG 1 for three LVIs with impact energies of 0.5 J, and impact coordinates of (150, 150), (150, 200), and (150, 300); Figure 7(b) indicates the signals captured by FBG 1 for three LVIs with impact coordinates of (150, 150) and impact energies of 0.5, 0.75, and 1.0 J.

Figure 7(a) shows that for three impacts with the same energy, the closer the impact is to the sensor, the faster the impact signal reaches it. The difference in their main peak is possibly due to the attenuation during propagation. Figure 7(b) shows that for three impacts at the same location, larger impact energy results in greater signal amplitude. These are because in LVIs, signals primarily propagate in the form of Lamb waves [33]. Lamb waves are dispersive, and their propagation velocity depends on the frequency of the waves, material properties, and plate thickness. Meanwhile, their amplitude is influenced by the impact energy, material properties, and thickness.

Therefore, the signal arrival time, peak time, and peak amplitude can be used to reflect the location and energy of LVIs. Since multiple local peaks appear in the time-domain signal, for the sake of convenience in the subsequent discussion, the selected local peaks are referred as feature peaks.

Sliding window peak detection is a commonly used peak detection algorithm. It detects local peaks effectively by moving a window along the data sequence. It has high computational efficiency, making it suitable for processing

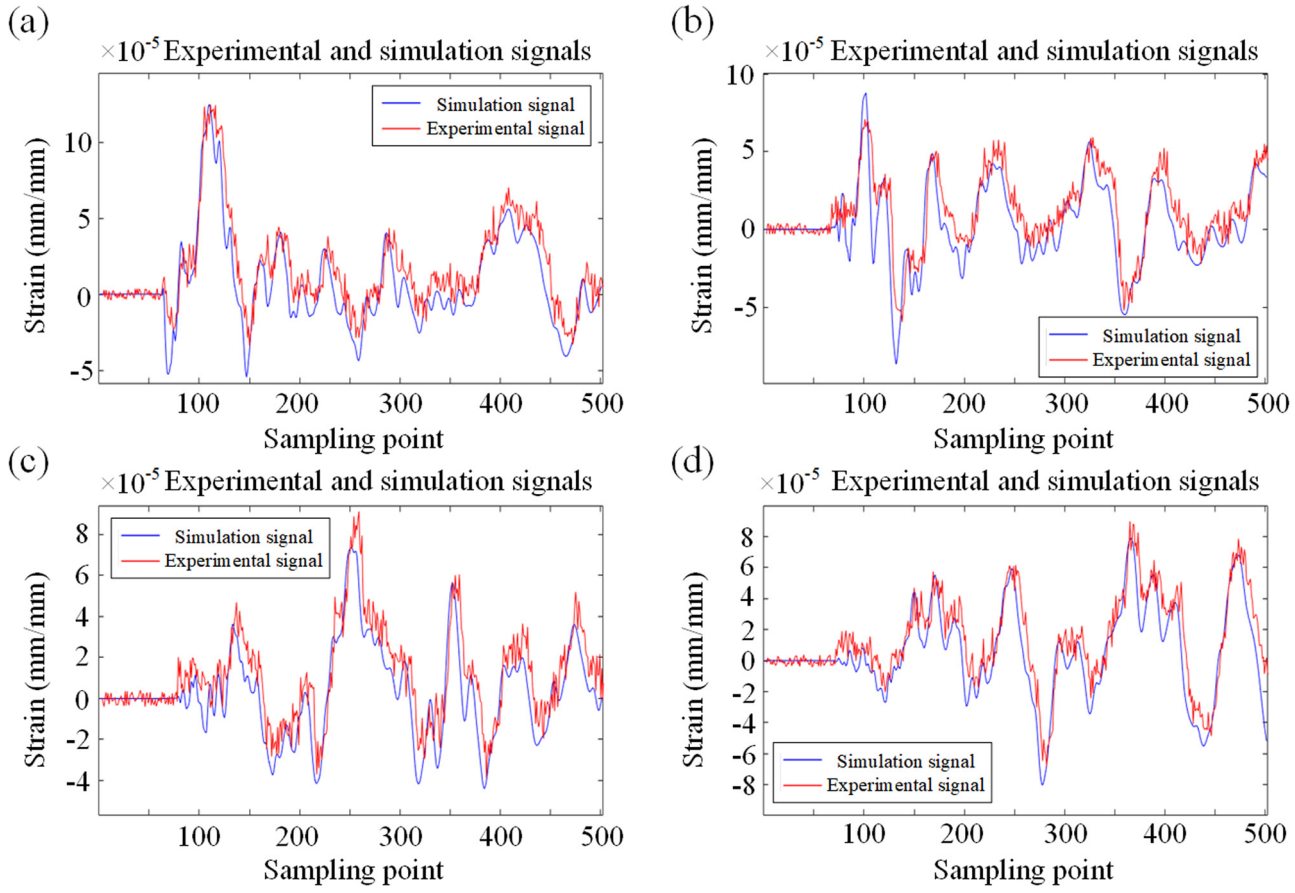

Figure 5: Experimental and simulation signals of initial impact at (a) FBG 1, (b) FBG 2, (c) FBG 3 and (d) FBG 4.

Table 2: Correlation coefficients of experimental and simulation signals

	Position (1)	Position (2)	Position (3)	Position (4)
Correlation index	0.8868	0.9034	0.8541	0.8231

large batches of data; it is versatile, as parameters can be adjusted to adapt to different waveforms; and it has strong anti-interference capability, allowing for data denoising. Considering the abundance and complexity of the signals, this method was chosen for peak detection in this study. The steps were as follows.

Step 1: Smooth the signal. Smoothing can reduce spikes in the signal and minimize unnecessary details. In this study, the moving average method from the "smooth" function in MATLAB was used for signal smoothing. In this method, the signal is smoothed by replacing the central data point of the window with the window's average value.

Step 2: Determine the size of the sliding window. The window size decides the influence of the selected peaks. A larger window can detect wider peaks but may miss narrow peaks, while a narrower window may introduce noise.

Step 3: Determine the step size. The step size decides the computational load and detection accuracy. A larger step can improve algorithm speed but may miss narrow peaks, while a smaller step may result in multiple detections of the same peak, wasting computation.

Step 4: Determine the threshold. By setting the lower limit of the peaks, the threshold decides the significance of the selected peaks.

Step 5: Based on the parameters mentioned above, a sliding window peak detection program was run in MATLAB to extract the peaks in the strain signal.

By continuously adjusting the parameters, the smoothing factor, window size, step size, and threshold were determined to be 10, 50, 2, and 2×10^{-5}. Figure 8(a) shows the peaks captured by sliding window peak detection (collected by FBG1 [150, 150, 0.5] as the impact parameters). It can be

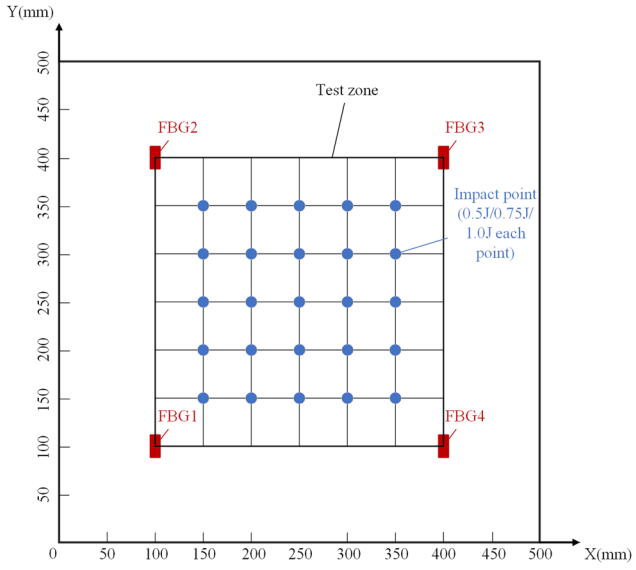

Figure 6: Neural network input dataset composition.

seen that the four main peaks of the signal were well detected. The purpose of the preliminary prediction was to explore the feasibility of using signal arrival time and feature peaks as signal features. Therefore, the more typical first peak was chosen as the feature peak tentatively, and the signal arrival time, the first peak time, and first peak amplitude were used as signal features, as shown in Figure 8(b).

2.4 Neural network training

Using the peak detection method described above to extract the signal arrival time, first peak time, and first peak amplitude of the four sensors from 75 samples, a 12-dimensional input features was formed as a result. Meanwhile, the impact's *x*-coordinate, *y*-coordinate, and energy were used as output values for prediction. However, due to the

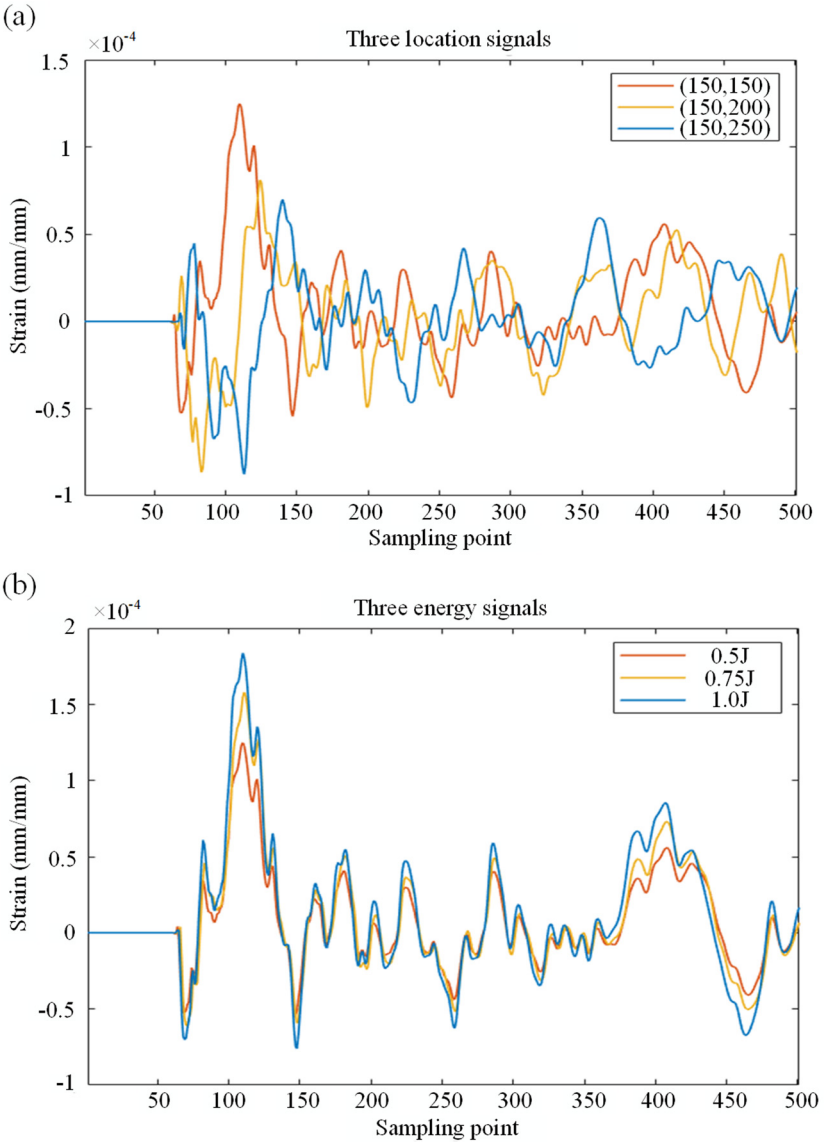

Figure 7: Strain time domain signals of strain signals with (a) different locations and (b) different energies.

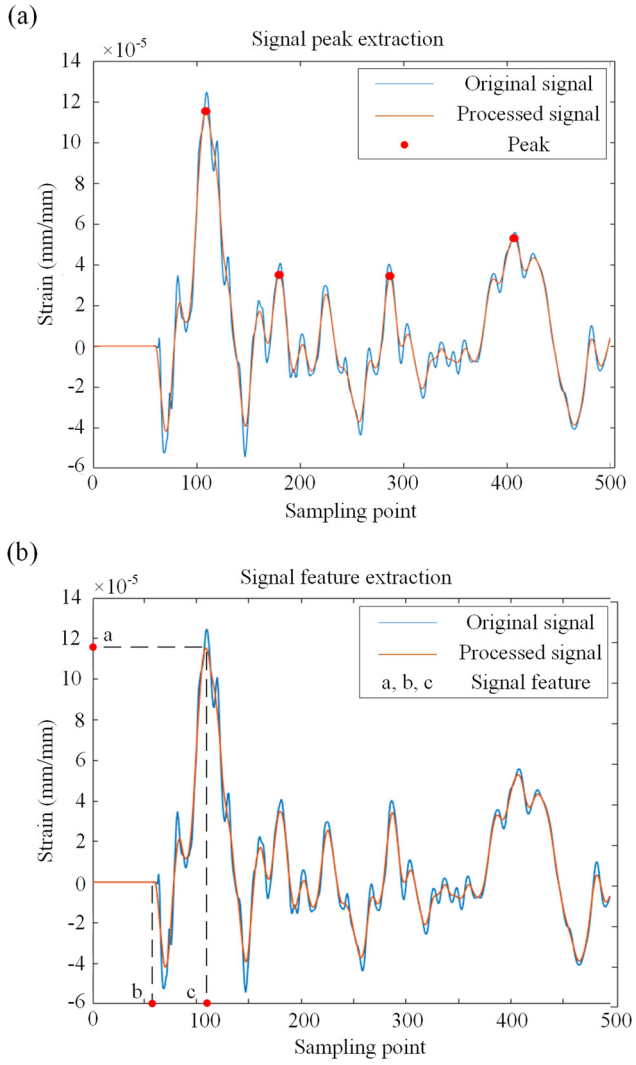

Figure 8: (a) Signal peak extraction and (b) signal feature extraction.

different data scales for coordinates and energy, larger feature values would dominate the gradient descent process, obscuring changes in smaller feature values. This made it challenging for the BP neural network to comprehensively learn the relationship between input and output. Therefore, before applying the target values, it is necessary to normalize the coordinates and energy separately to ensure that they have a similar scale range. The minimum–maximum normalization method, as shown in equation (1), was used to scale the data to the [0, 1] range:

$$x_{\text{normalized}} = \frac{x - \min(x)}{\max(x) - \min(x)}. \quad (1)$$

The BP neural network used in the research consisted of three layers: the input layer, hidden layer, and output layer, as illustrated in Figure 9. The detailed information is provided in Table 3. The number of hidden layers and

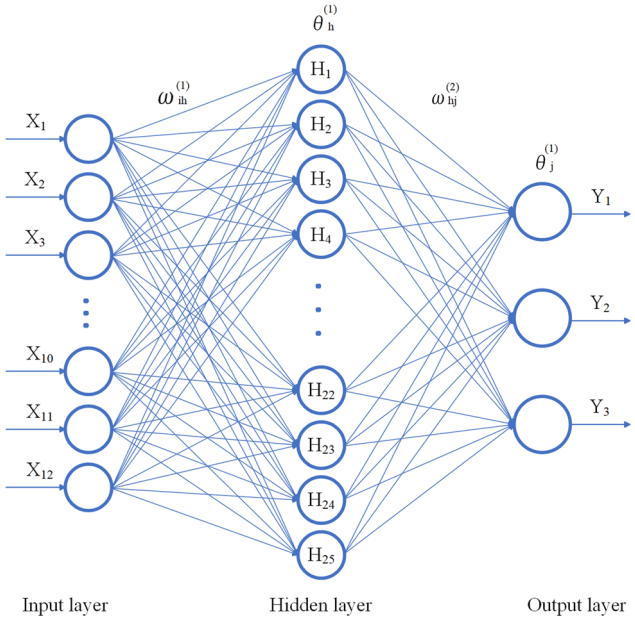

Figure 9: BP neural network topological structure.

nodes was determined after continuous testing. ω and θ represented weights and thresholds, respectively.

The input dataset was fed into the BP neural network first, before it was automatically divided into training (70%), validation (15%), and test (15%) sets. The training set was used to complete the iterative training process, as depicted in Figure 10. The validation set was used to prevent overfitting. After completing the neural network training, the test set error provided a reference for the neural network's ability to predict new data since it did not participate in the training process.

As shown in Figure 11(a), the validation set means squared error was minimized after the third iteration. This indicated that the neural network had achieved optimal generalization performance. Figure 11(b) presents the predictive curves and correlation coefficients of the best neural network

Table 3: Detailed neural network information

Neural network information		
Input layer	Node number	12
Hidden layer	Node number	25
	Activation function	Tansig
Output layer	Node number	3
	Activation function	Purelin
Training algorithm		Trainlm
Learning rate		0.0001
Number of training iterations		1,000
Training objective		0.0001

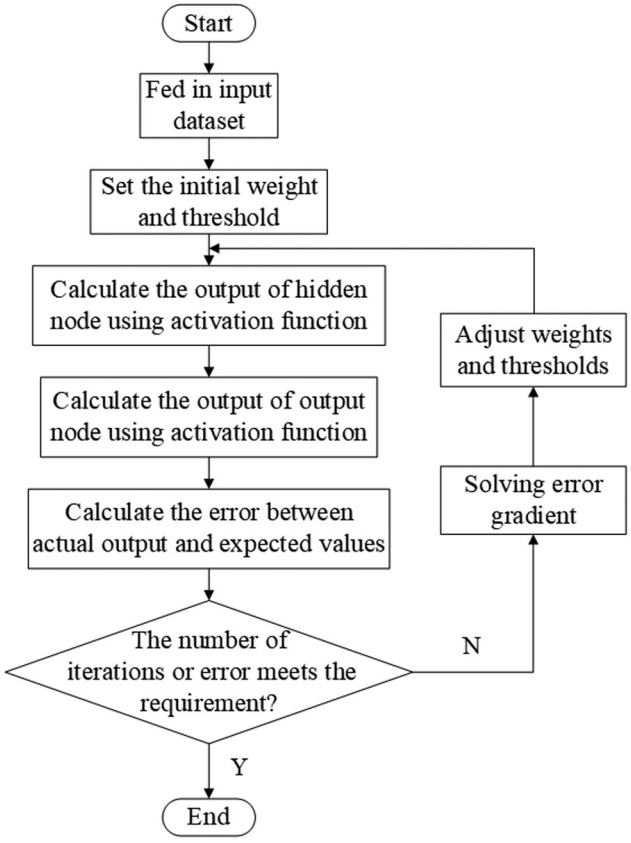

Figure 10: BP neural network training flowchart.

for the training, validation, test, and entire dataset. From the graph (IV), the neural network's *R*-value across the input set was 0.8551, which was close to 1, indicating good training performance.

2.5 Generalization ability validation

To validate the feasibility of the proposed method, it is essential to test the generalization capability of the trained neural network model, which signifies its predictive capacity for new data. To achieve this, within the test area, four LVIs with random locations and energies were designated as new test set. Their strain signals were obtained through the simulation model, and these signals were used to extract features as input for the neural network. Figure 12 depicts the actual and predicted locations by the neural network of four samples in the random test set. Table 4 provides the actual energies and predicted energies for each sample.

Through calculation, when using the trained neural network for predicting the test samples, the maximum error in location prediction was 19.9 mm, the minimum error was 1.9 mm, the average error was 13.2 mm, and the average error rate was 4.4%. For energy prediction, the maximum error was 0.131 J, the minimum error was 0.037 J, the average error was 0.076 J, and the average error rate was 15.2%, all of which reached a good level.

It is evident that using the signal arrival time, first peak time, and first peak amplitude in the strain signal

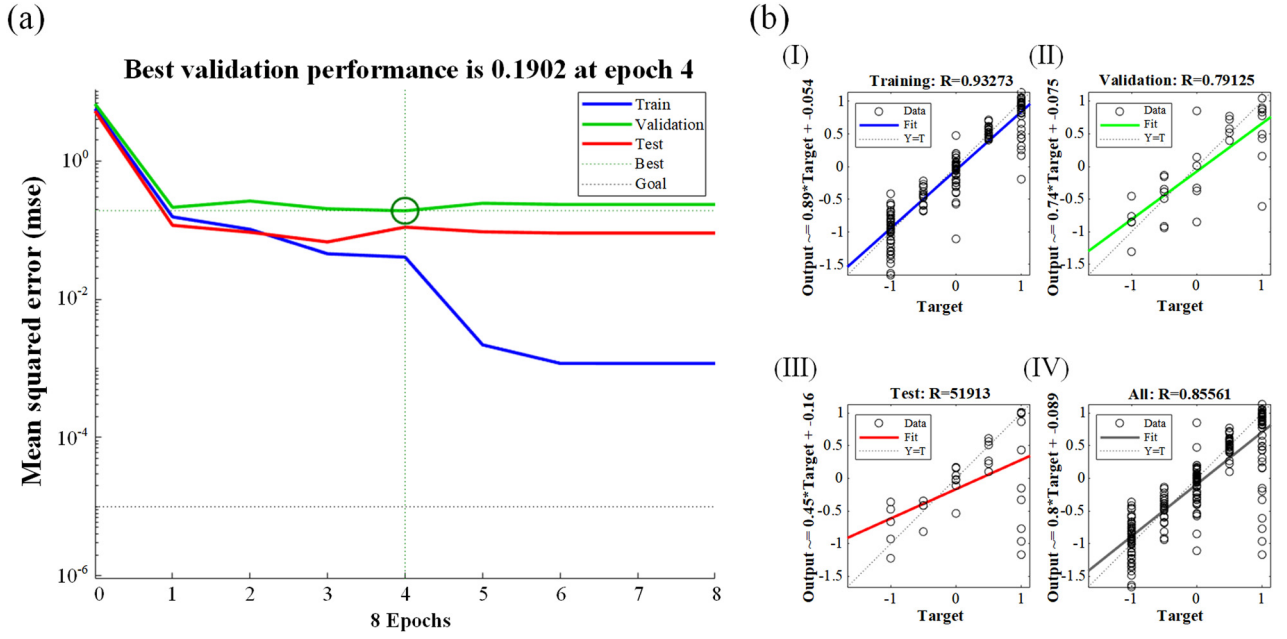

Figure 11: (a) BP neural network iteration process and (b) neural network fitting results in preliminary prediction.

as features to train the BP neural network allows for the prediction of LVI location and energy. However, in the preliminary prediction, the parameters of the sliding window peak detection were determined empirically, and the positions of the feature peaks were manually selected, leading to uncertainty in the formation of the input dataset, which subsequently affected the method's reliability in different scenarios.

3 Results and discussion

3.1 Selection of feature peaks

In the application of BP neural networks, the quality of the input dataset significantly affects the network's predictive capabilities [34,35]. Extracting features with higher relevance to the target signal to form the input dataset can help avoid the influence of noisy features. This allows the neural network to focus more on learning important features and patterns, enabling it to better understand the relationship between inputs and outputs. At the same time, it can prevent the neural network from paying excessive attention to secondary features in the training samples, thus preventing overfitting.

In this study, since the signal arrival time is fixed, the main issue in sample feature extraction is the selection of feature peaks. This involves how to preprocess the signal and extract an appropriate number and position of local peaks as feature peaks to better reflect changes in the target signal and, in turn, improve the predictive capabilities of BP neural network.

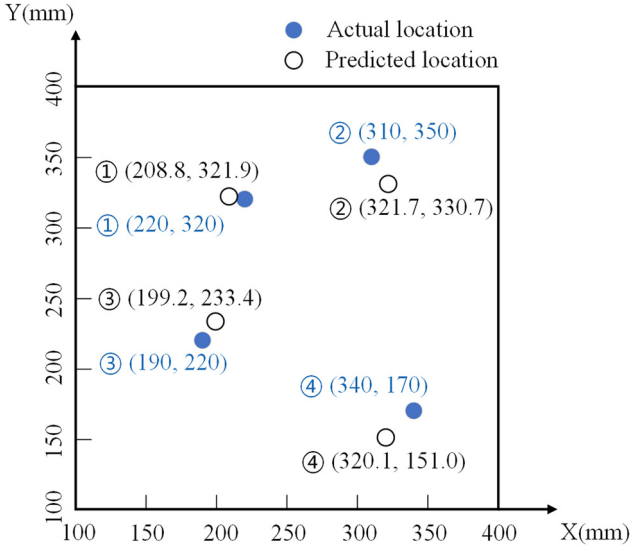

Figure 12: Actual and predicted impact location in preliminary prediction.

Extracting features with a stronger linear correlation to the target signal can make it easier for neural networks to perform pattern recognition. Therefore, multiple linear regression analysis can be used for an initial evaluation of the quality of the extracted features. Multiple linear regression analysis is a statistical method used to study the linear relationship between multiple independent variables and a continuous dependent variable. In the process of multiple linear regression analysis, a linear regression equation in the form of equation (2) is first formulated, and the sum of squared errors is set up using the least squares method as shown in equation (3). Then, a linear system of equations is obtained for the coefficients and constant term by taking partial derivatives, which is subsequently solved to find the linear regression equation.

$$\hat{Y} = b_0 + b_1X_1 + b_2X_2 + \ldots + b_mX_m, \tag{2}$$

$$Q = \sum(Y - \hat{Y})^2. \tag{3}$$

In multiple linear regression analysis, the goodness of fit for the model can be represented by the adjusted coefficient of determination (R^2). First, calculate the total sum of squares (SST) and the residual sum of squares (SSE). Then, calculate the coefficient of determination (R^2). Finally, obtain $\bar{R}^2$, as shown in equations (4)–(7). $\bar{R}^2$ ranges from 0 to 1, with values closer to 1 indicating a stronger linear relationship between the independent variables and the dependent variable. Moreover, due to the introduction of the degrees of freedom adjustment, $\bar{R}^2$ accounts for the impact of the number of independent variables on the fitting performance, which avoids overfitting caused by an excessive number of independent variables.

$$\text{SST} = \sum(y_i - \bar{y})^2, \tag{4}$$

$$\text{SSE} = \sum(y_i - \hat{y}_i)^2, \tag{5}$$

$$R^2 = 1 - \frac{\text{SSE}}{\text{SST}}, \tag{6}$$

$$\bar{R}^2 = 1 - (1 - R^2)\frac{n - 1}{n - p - 1}. \tag{7}$$

Table 4: Actual and predicted impact energy

Actual energy and predicted energy (J)				
Sample number	①	②	③	④
Actual energy	0.5	0.7	0.9	1
Predicted energy	0.5731	0.5689	0.8631	0.9356

Taking the first peak time and amplitude from the preliminary prediction as multivariate independent variables, and the *X*-coordinate, *Y*-coordinate, and energy of the target signal as dependent variables, to evaluate the correlation between the initial input dataset and the three target signals. Through calculation, when the first peak was used as the feature peak, the $\bar{R}^2$ between the input dataset and the target signals are as presented in Table 5.

It can be seen that in the preliminary prediction, the input dataset showed a good level of linear correlation with the *X*-coordinate of the impact, with a correlation coefficient of 0.90437. However, the initial input dataset had weaker correlations with the *Y*-coordinate and, particularly, the impact energy. This explained the relatively high average error rate in energy prediction for the test set in the preliminary prediction. As a result, it is necessary to optimize the input dataset, and the key is to optimize feature peak extraction.

Table 5: $\bar{R}^2$ between input dataset and target signals in preliminary prediction

Corresponding variables	$\bar{R}^2$
Input dataset and *X* coordinates	0.9043
Input dataset and *Y* coordinates	0.7343
Input dataset and energy	0.4991

3.2 Optimizing feature peak extraction using GA

GA is an optimization algorithm inspired by the principles of natural selection and genetics. It searches the solution space for the optimal or near-optimal solutions to a problem by simulating genetic operations such as inheritance, crossover, and mutation that occur in the process of biological evolution [36–38]. In the context of feature peak extraction from strain signals, multiple parameters including smoothing factor, window width, peak threshold, feature peak number, and feature peak position have a significant impact on the quality of extracted features. As a result, GA can be used to perform combinatorial optimization of these peak-seeking parameters. This can lead to the extraction of more typical feature peaks from the signal, thereby improving BP neural network training and enhancing its pattern recognition capabilities.

In the process of optimizing peak-seeking parameters for strain signal using GA, five parameters, including the smoothing factor, window width, peak threshold, feature peak number, and feature peak position, were selected to compose the genotype of each individual. In other words, each individual's chromosome carried five genes, and a region descriptor was used to define the data type and value range for each gene. The gene responsible for feature peak position was determined by a decimal parameter. When deciding which local peak to choose as a feature peak, this decimal number was converted into a binary number. Each bit in this binary number determined whether the corresponding local peak was selected. For example, the parameter "6" in binary is "110," indicating that, in feature peak selection, the first local peak is skipped (corresponding "0"), while the second and third local peaks can be chosen (corresponding "1").

Table 6: Values of hyperparameters in GA

GA parameter	Value
Population size	50
Maximum number of generations	50
Gene length	15
Generation gap	0.95
Crossover rate	0.7
Mutation rate	0.05

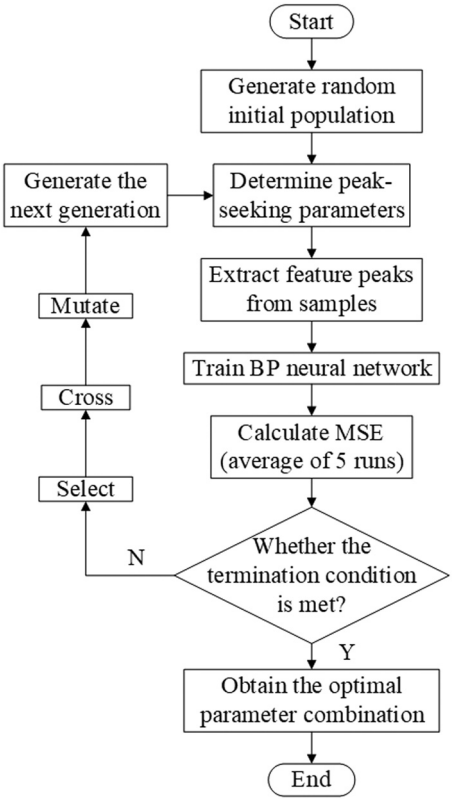

Figure 13: Optimized feature extraction method.

Table 7: Optimized peak-seeking parameters for sliding peak detection

Parameter	Optimized value
Smooth factor	16.2272
Window width	47
Peak threshold (mm)	0.000004
Peak quantity	2
Peak position	203

During the use of GA, hyperparameters including population size, maximum number of generations, gene length, and the rates of crossover and mutation have a significant impact on model performance. After continuous testing, the values of these hyperparameters in the GA were determined as shown in Table 6.

The steps of optimized feature extraction method using GA are shown in Figure 13. First, a random initial population is generated. Then, the peak-seeking parameters are determined by the genotype of each individual. Afterward, feature peaks are extracted from the samples using the peak-seeking parameters, and the neural network is trained using the training and validation sets. The fitness function is determined by the mean squared error (MSE) on the test set to represent the generalization performance of the trained neural network. To mitigate the impact of the random selection of initial weights and thresholds on MSE, the average MSE of five training runs is taken as the final MSE. Subsequently, if the maximum number of generations is not reached, selection, crossover, and mutation are performed to generate a new population. If the maximum number of generations is reached, iteration is stopped and the optimal individual is obtained.

After 50 iterations, the optimized results of peak-seeking parameters are shown in Table 7. Figure 14 takes the sample with impact parameters (150, 150, 0.5) as an example, showing the selected feature peaks when using the optimized peak-seeking parameters. It can be seen that after parameter optimization, the peak-seeking process enhanced the smoothing of the initial signal, highlighting the overall trend of the signal. More significantly, after optimization, the first two local peaks were selected as feature peaks together. This arrangement was difficult to discover without optimization.

A multivariate linear analysis was conducted on the feature peak dataset extracted after optimizing the peak-seeking parameters and the target signal. The correlation between the optimized dataset and the target signal was analyzed, resulting in $\bar{R}^2$ for the optimized dataset and the target signal, as shown in Table 8.

In comparison to non-optimized feature peak extraction, the new $\bar{R}^2$ for the X-coordinate of the impact point showed a slight increase (0.4%), while that for the Y-coordinate and impact energy increased by 15.7 and 60.3%, respectively, representing a substantial improvement. It can be seen that using GA to optimize peak-seeking parameters for the feature peak extraction, a stronger linear correlation between the input dataset and the target signal could be obtained. As a result, the quality of the input dataset was significantly enhanced, leading to a stronger predictive capability of the BP neural network.

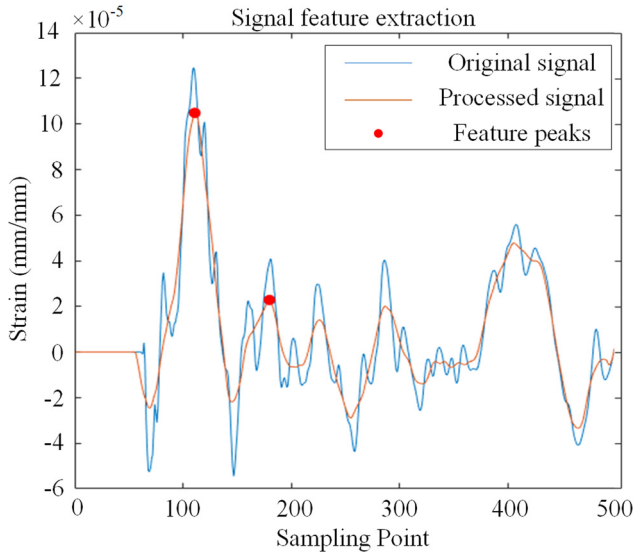

Figure 14: Selected feature peaks after parameter optimization.

3.3 Neural network training using optimized features

The optimized feature peak data and the original signal arrival time data were combined to form a new input dataset for the BP neural network, and the network was trained again. Through iterative updates of weights and thresholds, the network gradually reached the best level

Table 8: $\bar{R}^2$ between optimized dataset and target signals

Corresponding variables	$\bar{R}^2$	Increase rate (%)
Optimized peak dataset and X coordinates	0.9078	0.4
Optimized peak dataset and Y coordinates	0.0850	15.7
Optimized peak dataset and energy	0.8000	60.3

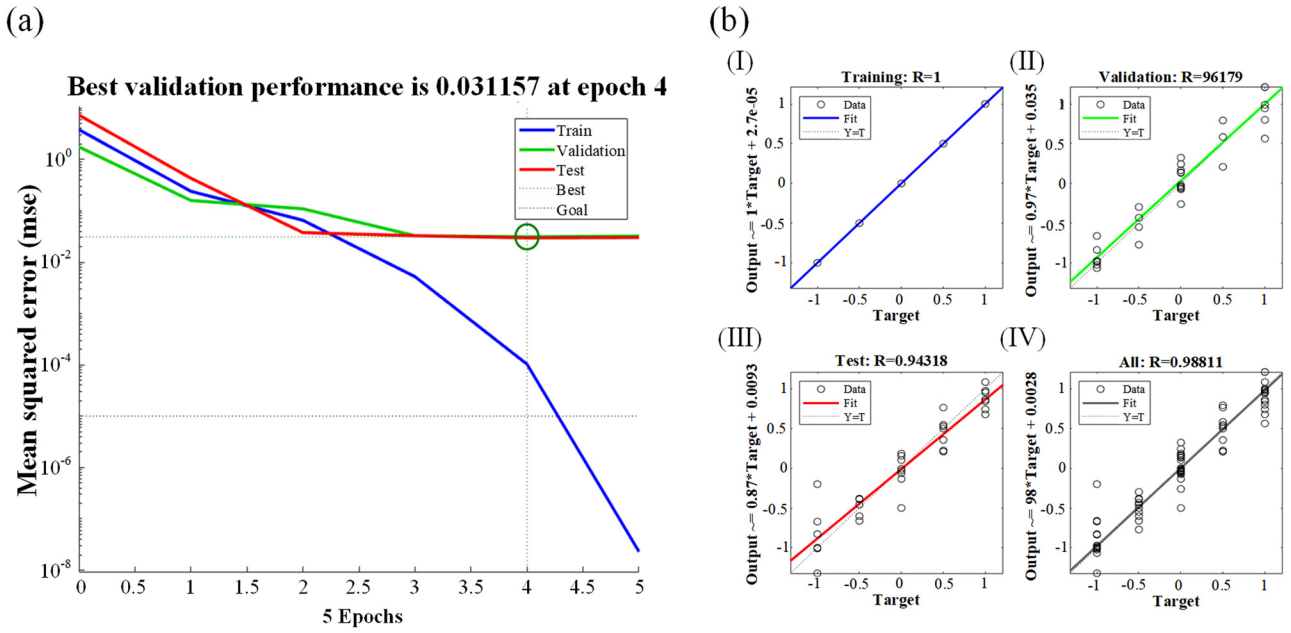

Figure 15: (a) BP neural network iteration process and (b) neural network fitting results after optimization.

of performance. As shown in Figure 15(a), the BP neural network achieved the lowest MSE on the validation set at the fifth iteration, indicating its best generalization ability, representing the optimal solution during the iteration process. Figure 15(b) shows that the neural network's coefficients of determination on the training set, validation set, test set, and the entire input set were all very close to 1. In particular, the *R*-value on the entire input set reached 0.98811, indicating a high degree of fit of the neural network to the input set.

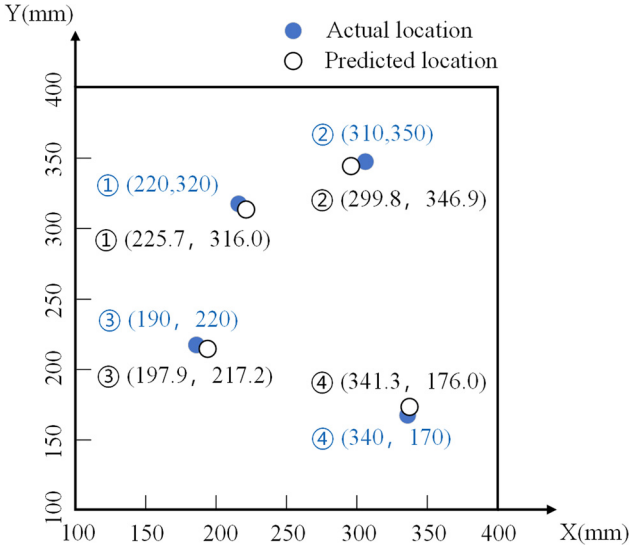

Figure 16: Actual and predicted impact location in optimized prediction.

3.4 Generalization ability validation of optimized neural network

To validate the generalization capability of BP neural network trained using the optimized input dataset, four test samples with random locations and energies were used to test the network. Using the optimized peak-seeking parameters for feature peak extraction from the strain signals, the actual locations and predicted locations of each sample in the test set are shown in Figure 16. The actual energies and predicted energies for each sample in the test set are presented in Table 9.

Through calculation, when using the optimized input dataset for prediction, the maximum error in location prediction was 10.2 mm, the minimum error was 1.3 mm, the average error was 5.1 mm, and the average error rate was 1.7%. For energy prediction, the maximum error was 0.054 J, the minimum error was 0.003 J, the average error was 0.030 J, and the average error rate was 6.0%. Compared to the results of the preliminary prediction, the average location error has decreased by 61.4% after optimizing feature

Table 9: Actual and predicted impact energy in optimized prediction

Actual energy and predicted energy (J)				
Sample number	①	②	③	④
Actual energy	0.5	0.7	0.9	1
Predicted energy	0.4648	0.7277	0.9029	0.9465

Table 10: Prediction results of GA optimization and other three optimization methods

Actual value	The predicted value of GA optimization	The predicted value of PSO optimization	The predicted value of SA optimization	The predicted value of GWO optimization
(220, 320, 0.5)	(225.7, 316.0, 0.465)	(216.6, 318.5, 0.466)	(203.2, 306.1, 0.534)	(200.9, 311.6, 0.507)
(310, 350, 0.7)	(299.8, 346.9, 0.782)	(315.9, 322.7, 0.726)	(307.8, 355.2, 0.735)	(316.7, 329.9, 0.604)
(190, 220, 0.9)	(197.9, 217.2, 0.903)	(174.3, 213.6, 0.901)	(205.2, 228.9, 0.977)	(197.2, 226.4, 0.970)
(340, 170, 1.0)	(341.3, 176.0, 0.946)	(352.2, 177.1, 1.132)	(351.2, 158.8, 1.036)	(334.9, 165.2, 0.994)

peak extraction, and the average energy error has decreased by 60.5%. This improvement in predictive accuracy for LVIs on composite materials demonstrates that applying GA to feature peak extraction from strain signals enhances the BP neural network's pattern recognition capabilities and results in better predictive performance.

3.5 Comparison of GA and other optimization methods

A comparison was made between parameter optimization of the sliding window peak detection based on GA and three other commonly used combinatorial optimization algorithms, aiming to explore the performance advantages of GA in the problem of peak-seeking parameter combinatorial optimization.

The three combinatorial optimization algorithms included in the comparison were PSO, simulated annealing (SA), and grey wolf optimization (GWO). All three algorithms were subjected to appropriate parameter tuning. For PSO, the particle swarm size was set to 50 and the number of iterations was 50. For SA, the maximum number of iterations was 100, the initial temperature was 100, and the initial guess was (0.00005, 10, 20, 2, 2). For GWO, the initial population size was 50 and the maximum number of iterations was 50.

Each of the three algorithms was separately applied to the peak-seeking parameters optimization, and the optimized parameters were then used to extract feature peaks from the strain signals. Subsequently, the new input dataset was used to train BP neural network as before, with the performance on random test sets serving as the evaluation metric. To ensure accuracy, during the iteration process of each algorithm, just like in GA optimization, the average of five training runs with the same set of parameters represented its final performance. Finally, the prediction results and performance metrics based on PSO, SA, and GWO optimization were obtained and compared with GA optimization, as shown in Tables 10 and 11.

According to the table, in all four metrics of location prediction, GA optimization outperformed the other three optimization methods, particularly in terms of average error, maximum error, and MSE. In the four metrics of energy prediction, GA optimization had an advantage in average error, maximum error, and MSE, and it was only slightly behind PSO optimization in minimum error. This result demonstrates the significant advantages of GA-optimized peak feature extraction in this type of problem. This advantage may be due to the unique stochastic mutation ability of GA, which means that in each iteration, one or more genes in an individual can change into other genes in a certain probability. This allows the simultaneous exploration of multiple potential solutions, increasing the chance of

Table 11: Performance metrics of GA optimization and other three optimization methods

Item compared		The predicted value of GA optimization	The predicted value of PSO optimization	The predicted value of SA optimization	The predicted value of GWO optimization
Location	Mean error	5.12 (best)	9.94	10.58	9.74
	Max error	10.24 (best)	27.31	16.84	20.06
	Min error	1.30 (best)	1.53	2.16	4.84
	MSE	33.2 (best)	160.03	133.96	128.29
Energy	Mean error	0.030 (best)	0.048	0.046	0.045
	Max error	0.054 (best)	0.132	0.077	0.096
	Min error	0.003	0.001 (best)	0.034	0.006
	MSE	0.001 (best)	0.005	0.002	0.004

escaping local optima and obtaining the global optimum. Therefore, compared to other optimization algorithms, GA has better prediction stability and global prediction capabilities. In conclusion, in the problem of optimizing feature peak extraction from strain signal, using the GA results in superior performance.

4 Conclusion

In this article, a new nanocomposite material SHM system based on FBG sensors and BP neural networks was established. Four sensors were employed, and the system collected time-domain strain signal features, including the signal arrival time, peak time, and peak amplitude during LVIs, resulting in a 12-dimensional input feature set. A BP neural network was employed for predicting the impact location and energy. In the context of feature peak extraction, GA was introduced to iteratively optimize peak-seeking parameters, leading to further improved prediction accuracy. Ultimately, the errors in impact location and energy prediction were reduced to 1.7 and 6.0%, respectively, demonstrating a good predictive performance.

This study provided a new approach for the joint prediction of the location and energy of LVIs on nanocomposite materials. The prediction method based on the signal arrival time and feature peaks in strain signals is simpler, more convenient, and easily applicable. The utilization of GA for parameter optimization demonstrates robust functionality and unique advantages. The new approach shows promising application prospects in the field of nanocomposite material SHM.

Acknowledgments: This work was supported by Key Laboratory of Icing and Anti/De-icing of CARDC (Grant No. IADL20210407), Natural Foundation of Shandong Province (Grant No. ZR2019BEE068), and Guangdong Basic and Applied Basic Research Foundation (Grant No. 2020A1515111208). The authors thank the referees of this paper for their valuable and very helpful comments.

Funding information: This work was supported by Key Laboratory of Icing and Anti/De-icing of CARDC (Grant No. IADL20210407), Natural Foundation of Shandong Province (Grant No. ZR2019BEE068), and Guangdong Basic and Applied Basic Research Foundation (Grant No. 2020A1515111208). The authors thank the referees of this article for their valuable and very helpful comments.

Author contributions: Zhiyuan Wang: conceptualization and data curation; Long Chen: writing – review and editing, methodology; Chenyang Zhu: formal analysis and methodology; Zhanqiang Liu: data curation, writing – review and editing; Qinghua Song: conceptualization, resources, and supervision. All authors have accepted responsibility for the entire content of this manuscript and approved its submission.

Conflict of interest: The authors state no conflict of interest.

References

[1] Li J, Zhang Z, Fu J, Liang Z, Hui D, Ramakrishnan KR. Effect of CNT film interleaves on the flexural properties and strength after impact of CFRP composites. Nanotechnol Rev. 2023;12:20230177. doi: 10.1515/ntrev-2023-0177.

[2] Hosseini M, Gaff M, Li H, Konvalinka P, Lair J, Hui D, et al. A review of the performance of fibre-reinforced composite laminates with carbon nanotubes. Nanotechnol Rev. 2023;12:20230164. doi: 10.1515/ntrev-2023-0164.

[3] Senthil K, Arockiarajan A, Palaninathan R, Santhosh B, Usha KM. Defects in composite structures: Its effects and prediction methods – a comprehensive review. Compos Struct. 2013;106:139–49. doi: 10.1016/j.compstruct.2013.06.008.

[4] Mitrevski T, Marshall IH, Thomson R, Jones R, Whittingham B. The effect of impactor shape on the impact response of composite laminates. Compos Struct. 2005;67(2):139–48. doi: 10.1016/j.compstruct.2004.09.007.

[5] Mitrevski T, Marshall IH, Thomson R. The influence of impactor shape on the damage to composite laminates. Compos Struct. 2006;76(1):116–22. doi: 10.1016/j.compstruct.2006.06.017.

[6] Oliver GA, Pereira JLJ, Francisco MB, Gomes GF. The influence of delamination parameters on the wavelet based damage index in CFRP structures. Mech Adv Mater Struct. 2023;30(6):1117–27. doi: 10.1080/15376494.2022.2028204.

[7] Oliver GA, Pereira JLJ, Francisco MB, Gomes GF. Wavelet transform-based damage identification in laminated composite beams based on modal and strain data. Mech Adv Mater Struct. 202331(19):4575–85. doi: 10.1080/15376494.2023.2202016.

[8] Ahmadian V, Beheshti Aval SB, Noori M, Wang T, Altabey WA. Comparative study of a newly proposed machine learning classification to detect damage occurrence in structures. Eng Appl Artif Intell. 2024;127:107226. doi: 10.1016/j.engappai.2023.107226.

[9] Sekine H, Fujimoto SE, Okabe T, Takeda N, Yokobori T. Structural health monitoring of cracked aircraft panels repaired with bonded patches using fiber Bragg grating sensors. Appl Compos Mater. 2006;13(2):87–98. doi: 10.1007/s10443-006-9011-1.

[10] Katunin A, Przystałka P. Damage assessment in composite plates using fractional wavelet transform of modal shapes with optimized selection of spatial wavelets. Eng Appl Artif Intell. 2014;30:73–85. doi: 10.1016/j.engappai.2014.01.003.

[11] Prasad SM, Krishnan B, Krishnamurthy CV. Structural health monitoring of composite structures using Lamb wave tomography. Smart Mater Struct. 2004;13(5):N73–9. doi: 10.1088/0964-1726/13/5/N01.

[12] Liu Q, Sun H, Wang T, Qing X. On-site health monitoring of composite bolted joint using built-in distributed eddy current sensor network. Materials. 2019;12(17):2019. doi: 10.3390/ma12172785.

[13] de Castro BA, Baptista FG, Ciampa F. Comparative analysis of signal processing techniques for impedance-based SHM applications in noisy environments. Mech Syst Signal Process. 2019;126:326–40. doi: 10.1016/j.ymssp.2019.02.034.
[14] Saeedifar M, Najafabadi MA, Zarouchas D, Toudeshky HH, Jalalvand M. Barely visible impact damage assessment in laminated composites using acoustic emission. Composites, Part B. 2018;152:180–92. doi: 10.1016/j.compositesb.2018.07.016.
[15] Loi G, Aymerich F, Porcu MC. Influence of sensor position and low-frequency modal shape on the sensitivity of vibro-acoustic modulation for impact damage detection in composite materials. J Compos Sci. 2022;6(7):190. doi: 10.3390/jcs6070190.
[16] Raut NP, Kolekar AB, Gombi SL. Optimization techniques for damage detection of composite structure: a review. Mater Today Proc. 2021;45:4830–4. doi: 10.1016/j.matpr.2021.01.295.
[17] Liu C, Xu X, Wu J, Zhu H, Wang C. Deep transfer learning-based damage detection of composite structures by fusing monitoring data with physical mechanism. Eng Appl Artif Intell. 2023;123:106245. doi: 10.1016/j.engappai.2023.106245.
[18] Moradi M, Broer A, Chiachío J, Benedictus R, Loutas TH, Zarouchas D. Intelligent health indicator construction for prognostics of composite structures utilizing a semi-supervised deep neural network and SHM data. Eng Appl Artif Intell. 2023;117:105502. doi: 10.1016/j.engappai.2022.105502.
[19] Johnson M. Waveform based clustering and classification of AE transients in composite laminates using principal component analysis. NDT E Int. 2002;35(6):367–76. doi: 10.1016/S0963-8695(02)00004-X.
[20] Jebieshia TR, Maiti DK, Maity D. Frequency-based damage assessment of composite members using unified particle swarm optimization. Int J Aeronaut Space Sci. 2020;21(1):63–79. doi: 10.1007/s42405-019-00187-0.
[21] Majumdar A, Maiti DK, Maity D. Damage assessment of truss structures from changes in natural frequencies using ant colony optimization. Appl Math Comput. 2012;218(19):9759–72. doi: 10.1016/j.amc.2012.03.031.
[22] Zang C, Imregun M. Structural damage detection using artificial neural networks and measured FRF data reduced *via* principal component projection. J Sound Vibrat. 2001;242(5):813–27. doi: 10.1006/jsvi.2000.3390.
[23] McCrory JP, Al-Jumaili SK, Crivelli D, Pearson MR, Eaton MJ, Featherston CA, et al. Damage classification in carbon fibre composites using acoustic emission: a comparison of three techniques. Composites, Part B. 2015;68:424–30. doi: 10.1016/j.compositesb.2014.08.046.
[24] Sante RDi. Fibre optic sensors for structural health monitoring of aircraft composite structures: recent advances and applications. Sensors. 2015;15(8):18666–713. doi: 10.3390/s150818666.
[25] Jinachandran S, Li H, Xi J, Prusty BG, Semenova Y, Farrell G, et al. Fabrication and characterization of a magnetized metal-encapsulated FBG sensor for structural health monitoring. IEEE Sens J. 2018;18(21):8739–46. doi: 10.1109/JSEN.2018.2866803.
[26] Kwon H, Park Y, Kim J-H, Kim C-G. Embedded fiber Bragg grating sensor-based wing load monitoring system for composite aircraft. Struct Health Monit. 2019;18(4):1337–51. doi: 10.1177/14759217198437720.
[27] Lopez-Higuera JM, Cobo LR, Incera AQ, Cobo A. Fiber optic sensors in structural health monitoring. J Lightwave Technol. 2011;29(4):587–608. doi: 10.1109/JLT.2011.2106479.
[28] Liu Q, Wang F, Xiao W, Cui J. Binary dynamic stochastic search algorithm with support vector regression for feature selection in low-velocity impact localization problem. Eng Appl Artif Intell. 2023;124:106554. doi: 10.1016/j.engappai.2023.106554.
[29] Califano A, Chandarana N, Grassia L, D'Amore A, Soutis C. Damage detection in composites by artificial neural networks trained by using in situ distributed strains. Appl Compos Mater. 2020;27(5):657–71. doi: 10.1007/s10443-020-09829-z.
[30] Panopoulou A, Roulias D, Loutas TH, Kostopoulos V. Health monitoring of aerospace structures using fibre Bragg gratings combined with advanced signal processing and pattern recognition techniques. Strain. 2012;48(3):267–77. doi: 10.1111/j.1475-1305.2011.00820.x.
[31] Shen LB, Tian LP. A static load position identification method for optical fiber-composite structures based on particle swarm optimization - back propagation neural network algorithm. Meas Control. 2022;56(3–4):820–31. doi: 10.1177/00202940221101673.
[32] Wen X, Sun Q, Li W, Ding G, Song C, Zhang J. Localization of low velocity impacts on CFRP laminates based on FBG sensors and BP neural networks. Mech Adv Mater Struct. 2022;29(26):5478–87. doi: 10.1080/15376494.2021.1956653.
[33] Su Z, Ye L. Fundamentals and analysis of Lamb waves. In: Su Z, Ye L, editors. Identification of damage using lamb waves: from fundamentals to applications. London, UK: Springer London; 2009. p. 15–58.
[34] Fukunaga K. Introduction to statistical pattern recognition. San Diego, CA: Elsevier Science; 2013.
[35] Jain AK, Duin RPW, Mao CJ. Statistical pattern recognition: a review. IEEE Trans Pattern Anal Mach Intell. 2000;22(1):4–37. doi: 10.1109/34.824819.
[36] De Jong K. Learning with genetic algorithms: an overview. Mach Learn. 1988;3(2):121–38. doi: 10.1007/BF00113894.
[37] Katoch S, Chauhan SS, Kumar V. A review on genetic algorithm: past, present, and future. Multimed Tools Appl. 2021;80(5):8091–126. doi: 10.1007/s11042-020-10139-6.
[38] Liepins GE, Hilliard MR. Genetic algorithms: foundations and applications. Ann Oper Res. 1989;21(1):31–57. doi: 10.1007/BF02022092.